Received: 9 September 2020 | Revised: 14 December 2020 | Accepted: 21 December 2020

DOI: 10.1002/nme.6614

RESEARCH ARTICLE

WILEY

A level set model for stress-dependent corrosion pit propagation

Richard Dekker[1] | **Frans P. van der Meer**[1] | **Johan Maljaars**[2,3] | **Lambertus J. Sluys**[1]

[1]Faculty of Civil Engineering and Geosciences, Delft University of Technology, Delft, The Netherlands

[2]Faculty of Built Environment, Eindhoven University of Technology, Eindhoven, The Netherlands

[3]Structural Reliability, TNO, Delft, The Netherlands

Correspondence
Richard Dekker, Faculty of Civil Engineering and Geosciences, Delft University of Technology, PO Box 5048, Delft 2600, The Netherlands.
Email: r.dekker-2@tudelft.nl

Abstract

A numerical model for corrosion pit propagation under mechanical loading is presented. The level set method is used for corrosion front tracking and also enables the domain to be split into a solid and a pit domain. In the pit the diffusion of atoms originating from the dissolution process occurring at the pit front is simulated. The model is capable of automatically capturing lacy cover formation due to the inclusion of activation control, diffusion control, and passivation. In the solid static equilibrium is solved to obtain strains and stresses. A parameter, dependent on the signs of the plastic strain increment and the back stress, is introduced to define the influence of plasticity on the corrosion rate. The model is used to study pit growth under electrochemical and mechanical loading. Under activation control combined with an elastic material response, pits propagate faster under constant loading than under cyclic loading. When plastic deformation occurs, cyclic loading can significantly increase the pit growth rate. Increasing the cyclic load frequency results in faster propagation due to kinematic hardening. Under diffusion control, mechanical loading does not influence the pit growth rate, given that the salt layer leading to diffusion control remains intact.

KEYWORDS

corrosion fatigue, level set method, multiphysics, pitting corrosion

1 | INTRODUCTION

Numerous metal structures are exposed to corrosion while simultaneously being subjected to mechanical loading. For example, offshore wind turbine parks are becoming increasingly popular as a means of energy production without using valuable space on land. The disadvantage is that the foundations of these structures, that is, the mono-pile or jacket structure, are exposed to a more corrosive environment compared with onshore wind turbines. Unfortunately, the effect of corrosion on the service lifetime is still relatively unknown, especially in the case of corrosion in combination with mechanical loading. Novel computer models that can simulate the combination of electrochemical and mechanical loading in metals could reduce this uncertainty, leading to more accurate lifetime predictions.

There are in general two major types of metal corrosion[1] in open-air. The first type is uniform corrosion in which there is a uniform loss in thickness over the surface exposed to the corrosive environment. The second type is local corrosion,

which can occur in the form of pitting. Pitting corrosion is most common among stainless steels and aluminum alloys,[2] but can also be found in nonstainless steels, for example in pipelines[3] and offshore structures.[4] pitting corrosion has generally a significantly larger impact on the lifetime of a structure than uniform corrosion. Pits may grow rather quickly and create stress concentration sites from which mechanically assisted cracks can initiate. To make things worse, the speed of corrosion increases in the presence of mechanical stress.[5] An additional challenge is posed by the fact that it is not always straightforward to define the size of a pit, because a perforated cover, known as a lacy cover, might hide the true pit size.[6] pitting corrosion can be defined by three different stages, namely, breakdown of the passive layer, metastable pit growth, and stable pit growth, where reaching stage three, stable pit growth, is most disastrous regarding structural failure.[2] This study focuses on the computational modeling of the stable pit growth stage.

Different methods can be found in literature to model stable corrosion pit propagation. These are finite volume models,[7,8] models that use the finite element method combined with adaptive meshing,[9-11] models using the extended finite element method (XFEM) combined with the level set method,[12-14] phase field models,[15-18] peridynamic models,[19] and cellular automata (CA) models.[20,21] Only two of these models considered lacy cover formation.[9,19] Furthermore, inclusion of the effect of a constant stress on the pit growth rate are included in a phase field model[18,22] for an elastic material and an elastic-plastic material,[16] and in a CA model[20] for an elastic-plastic material. Fatoba et al.[21] developed a CA model for corrosion that includes the effect of cyclic loading by using a cyclic stress–strain curve constructed from stabilized hysteresis loops. For both CA models, the effect of plastic strain on the corrosion process is taken into account by employing the Gutman equation[23] using the effective plastic strain as a variable to quantify the influence of plasticity on corrosion. However, a more general unified framework that can deal with pit growth under both constant and cyclic loading for an elastic-plastic material has not been found by the authors.

In this study, the level set method[24] is used in combination with the finite element method in order to simulate corrosion pit propagation. It avoids the need of remeshing which was required in other methods.[9-11] Furthermore, the level set method enables the domain to be easily split into a pit domain and a solid domain. In each domain a different set of equations is solved. In this study, it is shown that it is not required to use the full XFEM as was done in other studies that used the level set method.[12,13] Instead, a simple modification in integration scheme suffices, keeping the number of degrees of freedom (DOFs) per node constant, which is more in line with the phantom node version of XFEM.[25-27] This approach ensures that the two domains can be considered separately and therefore, for example, no unnecessary diffusion equations are solved in the solid domain. Furthermore, the influence of stress and strain on the pit growth velocity is included, where an isotropic and kinematic hardening plasticity model is employed such that the effect of cyclic plastic strain on the pit growth rate can be captured. For this a separate plasticity parameter is introduced that does not grow indefinitely in a stabilized cyclic response, which is another novel contribution in this article.

The article starts by presenting the description of the multiphysics problem to be solved, followed by the treatment of the mechanical behavior of the metal. Next, the corrosion behavior is discussed, in which activation controlled corrosion, diffusion controlled corrosion and passivation are addressed. In addition, the new state variable to indicate the state of plasticity is discussed. After that, the numerical framework is outlined with a description of the solution procedure. Finally, four numerical examples are given: a diffusion controlled pencil test, a study on the influence of the initial pit shape, a lacy cover formation problem and a study on the influence of mechanical loading on pit propagation.

2 | PROBLEM DESCRIPTION

A corrosion pit as visualized in Figure 1 is considered. The problem consist of two domains with a moving boundary, namely, the pit and the solid. The pit domain consists of an electrolyte which has the ability to transfer electrons. The pit front moves into the solid due to anodic dissolution, which means that a metal atom, indicated with M, leaves the solid and enters the pit solution while disposing itself of electrons. At the same time a cathodic reaction occurs that consumes these electrons in which for example hydrogen anions are converted into hydrogen gas. In this study, it is assumed that the cathodic reaction does not limit the rate of corrosion and thus only the anodic reaction is considered. Furthermore, a mechanical load is applied on the solid, resulting in stresses and strains, which can influence the pit growth rate.

The solid domain is the part in which the applied load is transferred. Here, static equilibrium should hold, which in the absence of any body forces, can be written as:

$$\nabla \cdot \boldsymbol{\sigma} = 0, \tag{1}$$

where $\boldsymbol{\sigma}$ is the mechanical stress and ∇ the differential operator.

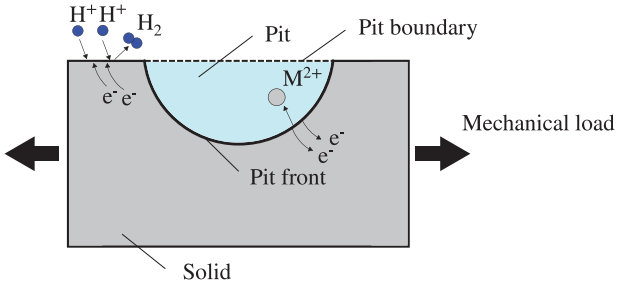

FIGURE 1 Schematic picture of the pit domain, the solid domain, and the pit front representing the corrosion process of a metal M and the applied mechanical loading (arrows)

In the pit domain there is a diffusion of metal atoms that originate from the solid. The concentration of metal atoms is therefore largest near the pit front and smallest near the pit boundary, which is the outside environment (Figure 1). The diffusion equation, in the absence of any source, is defined as follows:

$$\frac{\partial c}{\partial t}(\mathbf{x}, t) + \nabla \cdot \mathbf{J}(\mathbf{x}, t) = 0 \tag{2}$$

in which c is the concentration of atoms/ions, $\mathbf{J}$ is the flux of atoms, $\mathbf{x}$ is the location in the domain, and t is time. In this study, only the concentration of atoms of the metal itself is considered, however, inclusion of other species is possible as well.[11,28-30]

The pit front is not fixed in space, but propagates through the domain. The equilibrium between the flux of dissolved metal atoms and the velocity of the moving pit front is given by the Rankine–Hugoniot condition:[7,31]

$$\{\mathbf{J}(\mathbf{x}, t) + [c_{\text{solid}} - c(\mathbf{x}, t)]\mathbf{V}(\mathbf{x}, t)\} \cdot \mathbf{n}(\mathbf{x}, t) = 0. \tag{3}$$

Here, $\mathbf{V}$ is the front velocity, $\mathbf{n}$ is the unit normal vector that is perpendicular to the front, and c_{solid} is the concentration of atoms in the solid.

3 | MECHANICAL BEHAVIOUR

The mechanical load can be applied with a constant magnitude or in a cyclic fashion. Therefore, a plasticity model that includes both isotropic and kinematic hardening is used to capture plastic flow under cyclic loading. The elastic behavior simply follows from Hooke's law with Young's modulus E and Poisson ratio ν.

The Von Mises criterion is used to describe the yield surface:

$$f_{\text{vm}} = \sqrt{\frac{2}{3}(\mathbf{s} - \boldsymbol{\beta}) : (\mathbf{s} - \boldsymbol{\beta})} - \sigma_{\text{y}}, \tag{4}$$

where $\mathbf{s}$ and $\boldsymbol{\beta}$ are the deviatoric stresses and deviatoric back stresses, respectively. The yield stress σ_{y} is defined with a nonlinear isotropic hardening rule:[32]

$$\sigma_y = \sigma_0 + Q_\infty \left(1 - \mathrm{e}^{-b\bar{\epsilon}_{\text{p}}}\right), \tag{5}$$

where σ_0 is the initial yield stress, Q_∞ the limit value for the yield stress increase and b is a measure for the rate of change of the yield surface. The increment in equivalent plastic strain $\mathrm{d}\bar{\epsilon}_{\text{p}}$ is given as:

$$\mathrm{d}\bar{\epsilon}_{\text{p}} = \sqrt{\frac{2}{3}\mathrm{d}\boldsymbol{\epsilon}_{\text{p}} : \mathrm{d}\boldsymbol{\epsilon}_{\text{p}}}, \tag{6}$$

where $\mathrm{d}\boldsymbol{\epsilon}_{\text{p}}$ is the plastic strain increment. The kinematic hardening rule is given by Chaboche[33]:

$$\mathrm{d}\boldsymbol{\beta} = \frac{2}{3}C\mathrm{d}\boldsymbol{\epsilon}_{\text{p}} - \gamma\boldsymbol{\beta}\mathrm{d}\bar{\epsilon}_{\text{p}}, \tag{7}$$

where C is the linear and γ is the nonlinear kinematic hardening coefficient.

4 | CORROSION BEHAVIOUR

A distinction between three different regimes can be made when looking at stable pitting corrosion. First, there is activation controlled corrosion in which the corrosion speed is given and serves as a boundary condition for the diffusion problem. The second regime occurs when a certain saturation concentration c_{sat} is reached on the inside of the pit front at which point a salt layer forms on the front. The speed of the corrosion process then depends on the speed with which the metal atoms diffuse away from the front surface and it is therefore called diffusion controlled corrosion. The third option is simply passivation, which means that the corrosion process has come to a halt. The three regimes, and how they use Equation (3), are discussed next.

4.1 | Activation control

In activation control the rate with which the pit grows depends on the rate of the corrosion reaction, which is defined by the anodic current density i_{a}. The Butlet–Volmer equation or the Tafel equation can be used to compute the current density as function of the applied potential.[7,8,12] However, in this study, the anodic current density is used as an input instead of the applied potential. It is assumed that the current density acts perpendicular to the front, which means that the following equation holds:

$$\mathbf{i}_{\text{a}}(\mathbf{x}, t) = \mathbf{n}(\mathbf{x}, t)\, i_{\text{a}}. \tag{8}$$

The electric current at a dissolving electrode is proportional to the mass being dissolved per time instant as stated by Faraday's law:

$$\mathbf{i}_{\text{a}}(\mathbf{x}, t) = \mathbf{V}(\mathbf{x}, t)\, c_{\text{solid}} z F, \tag{9}$$

where F is Faraday's number and z the number of electrons involved. For a given i_{a} this equation can be rewritten to obtain an expression for the front velocity:

$$\mathbf{V}(\mathbf{x}, t) = \frac{i_{\text{a}} \mathbf{n}(\mathbf{x}, t)}{c_{\text{solid}} z F}. \tag{10}$$

It is assumed that movement of dissolved ions is diffusion dominated,[34] which means that the flux is represented by Fick's law:

$$\mathbf{J}(\mathbf{x}, t) = -D \nabla c(\mathbf{x}, t), \tag{11}$$

where D is the diffusion coefficient of the metal in the electrolyte. Substituting Equation (11) into Equation (3) gives

$$\{-D \nabla c(\mathbf{x}, t) + [c_{\text{solid}} - c(\mathbf{x}, t)]\, \mathbf{V}(\mathbf{x}, t)\} \cdot \mathbf{n}(\mathbf{x}, t) = 0, \tag{12}$$

where the velocity $\mathbf{V}$ is given by Equation (10). Thus, in the case of activation control, the front condition acts as a mixed or Robin boundary condition which depends on a front velocity that is known a priori.

4.1.1 | Mechanical stress-dependent corrosion rate

According to Gutman,[23] the anodic current density of a pure metal is influenced by the amount of plastic strain $\overline{p}$ and hydrostatic stress σ_{H} through the following relation:

$$i_{\text{a}} \to i_{\text{a}} \left(\frac{\overline{p}}{\epsilon_0} + 1 \right) \exp\left(\frac{|\sigma_{\text{H}}| V_{\text{m}}}{RT} \right), \tag{13}$$

where ϵ_0 is the initial yield strain, V_m is the molar volume of the solid metal, R is the universal gas constant, and T the temperature. According to this equation, an increase in the amount of plasticity or an increase in the absolute value of the hydrostatic stress results in a faster corrosion rate. When considering a one-dimensional (1D) case, $\overline{p}$ is simply equal to the plastic strain. In a multidimensional case, under a constant or an increasing applied stress, the equivalent plastic strain $\overline{\epsilon}_p$ could substitute $\overline{p}$ as in Reference 20.

However, there is a problem in using $\overline{\epsilon}_p$ as indicator for the amount of plastic strain in the case of cyclic loading. According to Gutman, an increase in dislocation density and in dislocation pile up, accelerates the corrosion rate. Due to the combination of Equation (6), which states that the equivalent plastic strain cannot decrease in value, and the presence of kinematic hardening, the equivalent plastic strain will keep on increasing whenever there is a plastic strain increment. This means that $\overline{\epsilon}_p$ increases in value even when the global cyclic response has stabilized. In reality, kinematic hardening under cyclic loading represents dislocations moving back and forth,[35] meaning that the largest pile up can decrease when reversed loading starts. Therefore, under cyclic loading, $\overline{\epsilon}_p$ from Equation (6) is not a correct measure for dislocation pile up. Note that a previous numerical study on corrosion pit growth that only considered cyclic loading did not encounter this problem because stabilized plasticity relations were used,[21] although the physical meaning of $\overline{\epsilon}_p$ in such equations is debatable.

To ensure the presented plasticity relations can still be used, a new parameter, defined as the equivalent dislocation strain $\overline{\epsilon}_d$, is introduced:

$$d\overline{\epsilon}_d = \int_0^{d\overline{\epsilon}_p} \operatorname{sgn}\left(d\boldsymbol{\epsilon}_p \cdot \boldsymbol{\beta}\right) dx. \tag{14}$$

The parameter $\overline{\epsilon}_d$ can, unlike $\overline{\epsilon}_p$, increase or decrease in magnitude. It decreases in value when the plastic strain increment acts in the opposite direction of the back stress, which could occur under cyclic loading. In the case of a monotonically increasing stress, $\overline{\epsilon}_d$ is equal to $\overline{\epsilon}_p$. It should be emphasized that the mechanical behavior is still determined by using $\overline{\epsilon}_p$, and is therefore not affected by $\overline{\epsilon}_d$. The parameter $\overline{\epsilon}_d$ is only used in Equation (13) as a substitute of $\overline{p}$ in order to compute the increase in the anodic current density.

Figure 2 shows the evolution of $\overline{\epsilon}_d$ and $\overline{\epsilon}_p$ under monotonic and cyclic loading. For cyclic load the maximum value of both parameters for each loading cycle is plotted against the number of loading cycles. Under monotonic load the two plasticity measures remain exactly equal. However, there is a significant difference between the two when considering cyclic loading. $\overline{\epsilon}_p/\epsilon_0$ reaches values of over 300, while $\overline{\epsilon}_d/\epsilon_0$ reaches values of around 35 and remains relatively constant after 50 cycles, which is the desired characteristic behavior for $\overline{p}$ in Equation (13) when the cyclic response stabilizes.

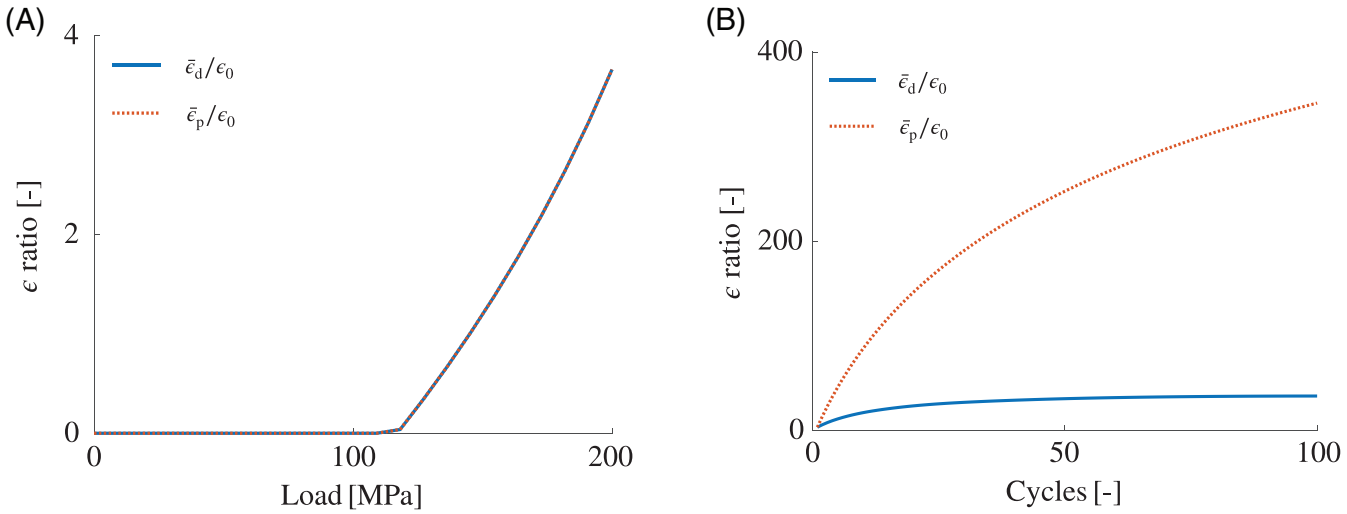

FIGURE 2 Development of $\overline{\epsilon}_d$ and $\overline{\epsilon}_p$ for a single element test under (A) a monotonic applied load, and (B) under cyclic loading with a maximum applied stress of 200 Mpa and a load ratio of −1. The material parameters can be found in Table 1

4.2 | Diffusion control

Diffusion control occurs once the saturation concentration c_{sat} is reached on the inside of the pit front, which leads to the formation of a salt layer. Due to this salt layer, the concentration on the inside of the pit front remains constant at c_{sat}. Therefore, this concentration is applied as a Dirichlet or essential boundary condition on the inside of the front, which means that it has been assumed that the salt layer has zero thickness. Consequently, Equation (3) is no longer applied as a boundary condition, but is used to determine the front velocity once the concentration distribution has been computed:

$$\mathbf{V}(\mathbf{x}, t) = \frac{D\nabla c \cdot \mathbf{n}(\mathbf{x}, t)}{c_{\text{solid}} - c_{\text{sat}}}. \tag{15}$$

Note that in this case the front velocity is no longer dependent on i_a and thus plastic strain and hydrostatic stress do not influence the front velocity.

4.3 | Passivation

In this study, a simple passivation model has been used in which corrosion process comes to a halt once the front concentration in the pit is smaller or equal to a passivation concentration c_{pas}.[6] In this case the front velocity is zero and Equation (3) reduces to:

$$\mathbf{J}(\mathbf{x}, t) = \mathbf{0}. \tag{16}$$

5 | NUMERICAL FRAMEWORK

The mechanically assisted pitting corrosion process is simulated by combining the finite element method with the level set method, which is visualized in Figure 3. In the level set method a front is tracked implicitly by assigning every node a signed distance value ϕ, of which the magnitude is equal to the shortest distance between the node and the front. A positive value indicates that the node is present in the solid, while if the value is negative or equal to zero the node is located in the pit.

The solid domain Ω_S and the pit domain Ω_P are constructed by taking elements located on respective sides of the front. However, some elements are cut by the front and are thus present in both the pit and the solid domain. This is solved by only integrating the area that is on the outside of the front ($\phi > 0$) for the solid domain and inside the front for the pit domain. The specific integration areas are created by triangular partitioning as shown in Figure 3. The elements through which a section of the front is present, are called the front elements. The nodes of these front elements are defined as the front nodes. Furthermore, having the location of the front by means of the signed distance value, line elements can be introduced in the elements that are crossed by the front. These line elements are assigned front integration points, indicated with solid squares in Figure 3, at which the regime of corrosion, the local front velocity, the stresses, and the strains are determined.

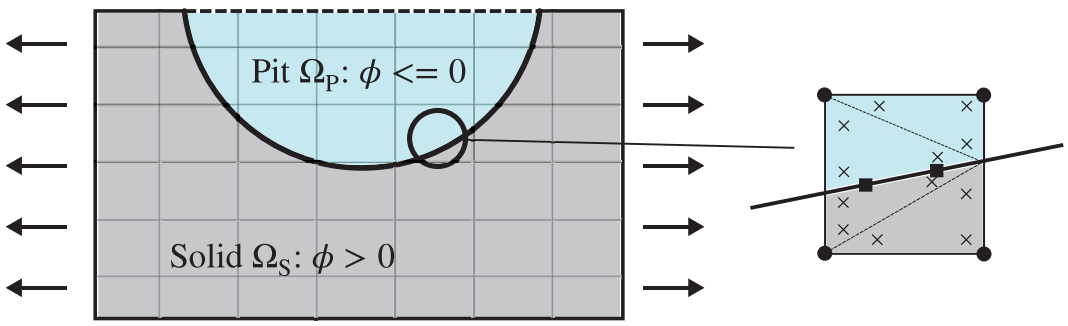

FIGURE 3 A corrosion pit under mechanical stress in a finite element and level set method numerical framework. Elements cut by the front are both present in the solid and the pit, but use different integration schemes depending on the domain

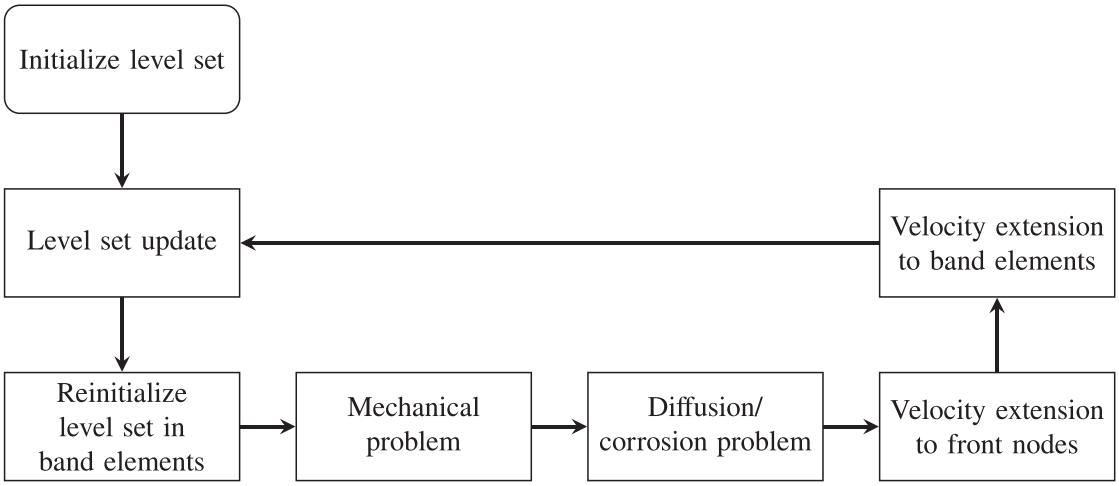

FIGURE 4 Flow diagram of the mechanically assisted pitting corrosion model

The solution is computed by means of a staggered approach in which there is a total of seven different steps. The order of the steps are indicated in the flow diagram in Figure 4. For corrosion without an applied mechanical stress, the mechanical problem step is simply skipped.

When considering cyclic mechanical loading, the solution procedure does not involve any additional step in the flow diagram. However, the time increment is now coupled to the load cycle frequency and thus the mechanical load increment. For example, the fatigue cycle period is 10 s for a fatigue cycle frequency of 0.1 Hz. When using 10 load steps per cycle for this given frequency, it means that the time increment per load step should be equal to 1 s. In the remainder of this section, the different parts of the numerical framework are discussed in more detail.

5.1 | Level set update

It is required that the velocity at the nodes is known in order to update the level set. For the very first level set update, the velocity is simply zero. The level set is updated explicitly by means of the following equation:

$$\phi^{t+\Delta t} = \phi^{t} - V_{n}\Delta t. \tag{17}$$

The time increment is defined by the Courant–Friedrichs–Lewy (CFL) condition to ensure stability of the solution.[36] In the case of cyclic loading, the time increment per load step should be lower than the CFL condition. If this is not the case, the number of load steps per cycle simply has to be increased.

At each level set update, the front moves outward. This means that after every update the old front lines are removed and new ones are introduced. Where necessary, concentration DOF are added on the nodes and displacement DOF removed. In addition, the integration areas created by triangulation are updated.

5.2 | Level set reinitialization

Reinitialization of the level set is performed to ensure that the signed distance property remains satisfied at every node. This property is defined by the following relation, which is known as the Eikonal equation:

$$|\nabla\phi| - 1 = 0. \tag{18}$$

In this study, two different methods for reinitialization were considered. The first one uses the fast marching method[36] which is a time efficient algorithm. However, this method, without the use of a shadow or dual mesh, can only be employed for either a structured mesh or a mesh composed of linear triangular elements as done by van der Meer et al.[37]

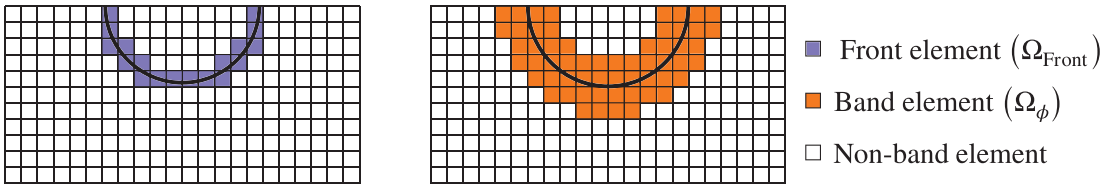

FIGURE 5 Front and band elements around the pit front

The other method for reinitialization follows the procedure by Adams et al.,[38] where the least square residual of Equation (18) is minimized, followed by Picard linearization and then transformed to a weak form. The method of using field equations for reinitialization can be used for any type of mesh. However, solving a system of equations is more expensive than using a fast marching algorithm. Fortunately, the computation time can be significantly reduced by only considering a band of elements around the pit front as is shown in Figure 5. In addition, it is generally not necessary to perform the reinitialization of the level set every time the level set is updated, but this can be done every five or ten steps, depending on the complexity of the front shape, to ensure that ϕ remains approximately equal to a signed distance function.[36] In this article it is assumed that the signed distance values at the nodes belonging to front elements ϕ_{Front} are known and can therefore be used as Dirichlet boundary conditions. This simplifies the weak form significantly:

$$\int_{\Omega_\phi} \nabla\phi^m \cdot \nabla\psi \mathrm{d}\Omega = \int_{\Omega_\phi} \nabla\psi \cdot \frac{\nabla\phi^{m-1}}{|\nabla\phi^{m-1}|}\mathrm{d}\Omega \text{ with } \phi^m = \phi_{\text{Front}} \text{ on } \Omega_{\text{Front}}, \tag{19}$$

where ψ is the test function, Ω_ϕ the domain of the band and Ω_{front} the domain of the front elements (Figure 5). The superscript m indicates the unknown signed distance solution for the current iteration step and the superscript $m-1$ from the previous. Note that the size of the band depends on the reinitialization interval. The reinitialization equation is solved iteratively until the signed distance value is converged. The resulting system of equations has a discretized elemental reinitialization stiffness contribution that is given by:

$$\mathbf{K}_{\text{re}} = \int_{\Omega_\phi} \mathbf{B}^{\mathrm{T}}\mathbf{B}\mathrm{d}\Omega, \tag{20}$$

where $\mathbf{B}$ are the gradients of the shape functions $\mathbf{N}$ which are used to discretize the test function and the state variable. The elemental reinitialization external vector contribution is defined as:

$$\mathbf{f}_{\text{re}} = \int_{\Omega_\phi} \mathbf{B}^{\mathrm{T}} \frac{\mathbf{B}^{\mathrm{T}}\boldsymbol{\phi}^{m-1}}{\left|\mathbf{B}^{\mathrm{T}}\boldsymbol{\phi}^{m-1}\right|}\mathrm{d}\Omega. \tag{21}$$

5.3 | Mechanical problem

The mechanical problem solves the static equilibrium given in Equation (1), of which the weak form is defined as:

$$\int_{\Omega_{\mathrm{S}}} \sigma : \nabla\psi \mathrm{d}\Omega = \int_{\mathrm{S}} \tau \cdot \psi \mathrm{dS} \tag{22}$$

with prescribed displacements or tractions τ on the domain boundary S_u or S_τ, respectively. This equation is solved only in the solid domain with the nodal displacements as unknowns. Due to the inclusion of plasticity the mechanical problem is solved with the Newton–Raphson method[39-41] which minimizes the difference between the internal force vector $\mathbf{f}^{\text{int}}_{\text{mech}}$ and the external force vector $\mathbf{f}^{\text{ext}}_{\text{mech}}$. The resulting system of equations consists of a discretized elemental stiffness contribution:

$$\mathbf{K}_{\text{Mech}} = \int_{\Omega_{\mathrm{S}}} \mathbf{B}^{\mathrm{T}}\mathbf{D}_{\text{stiff}}\mathbf{B}\mathrm{d}\Omega, \tag{23}$$

where $\mathbf{D}_{\text{stiff}}$ is the consistent tangent stiffness. The discretized elemental external vector contribution is defined as:

$$\mathbf{f}_{\text{Mech}}^{\text{ext}} = \int_{S_r} \mathbf{N}^{\text{T}} \boldsymbol{\tau} \text{dS} \tag{24}$$

and the elemental internal vector contribution is given by:

$$\mathbf{f}_{\text{Mech}}^{\text{int}} = \int_{\Omega_S} \mathbf{B}^{\text{T}} \boldsymbol{\sigma} \text{d}\Omega. \tag{25}$$

In order for the corrosion problem to use the mechanical result, σ_{H} and $\bar{\epsilon}_{\text{d}}$ should be known at the front integration points. The value of these quantities can strongly depend on the mesh size. For example, decreasing the mesh size around a stress concentration site significantly increases the stress as well as the amount of plastic strain. Consequently, the corrosion speed up for a fine mesh is larger than for a coarser mesh. Therefore, a nonlocal approach is used to compute these quantities in order to avoid a mesh dependency through local plastic behavior by introducing an extra length-scale.[42,43] The nonlocal quantities are computed as the weighted average values from solid bulk integration points using the following weight function:

$$w = \frac{1}{(\pi r_{\text{w}})^2} \exp\left(-\frac{l_{\text{w}}^2}{2r_{\text{w}}^2}\right), \tag{26}$$

where l_{w} is the distance between the bulk and front integration point, The length scale r_{w} defines both the search radius around a front integration point and the rate of decay of the weight function, and has generally a value of two to three times the element size.

Note that the bulk integration scheme within a front element changes once the front moves. In order to transfer the history data, the old integration points are first extrapolated to the nodes, followed by interpolation to the new integration points.[41]

5.4 | Diffusion/corrosion problem

As explained in Section 4, there are three regimes for corrosion, namely, activation control, diffusion control, and passivation, where different points along the front can be in different regimes. The regime of corrosion is determined for each time step according to the following scheme:

1. Set all the front integration points to activation control except the ones that were passivated in the previous time step and are thus under passivation control. Include Equation (13) when mechanical loading is considered.
2. Solve for the concentrations in the pit domain given the current configuration of control of each front integration point.
3. Check the front concentration c_{front} for each front integration point.
   - If $c_{\text{front}} \geq c_{\text{sat}}$ switch to diffusion control for the front integration point in consideration.
   - If $c_{\text{front}} \leq c_{\text{pas}}$ switch to passivation for the front integration point in consideration.
4. The final concentration solution is computed if the regime of corrosion is not changed for any of the front integration points in step 3. If not, go back to 2 and repeat the process.

Each corrosion regime results in different boundary conditions, which result in extra stiffness and external load vector terms. In activation control there is a Robin boundary condition, given in Equation (12), which can be rewritten to:

$$-\mathbf{J} \cdot \mathbf{n} = c_{\text{solid}} \text{V}_{\text{n}} - c \text{V}_{\text{n}} \tag{27}$$

in which the following relation has been used:

$$\mathbf{V} = \text{V}_{\text{n}} \mathbf{n}. \tag{28}$$

In diffusion control a Dirichlet boundary condition is applied at the pit front, which in this article is done by using Nitsche's method for embedded surfaces.[44] In the case of passivation, no special action is required.

The weak form of the diffusion equation given in Equation (2), extended with the Robin and Nitsche boundary conditions, is given by:

$$\int_{\Omega_P} \psi \frac{\partial c}{\partial t} \mathrm{d}\Omega + \int_{\Omega_P} D\nabla c \cdot \nabla\psi \mathrm{d}\Omega + \int_{S_A} c \mathrm{V_n} \psi \mathrm{dS} \quad - \int_{S_D} D\psi \nabla c \cdot \mathbf{n} \mathrm{dS} - \int_{S_D} D\left(c - c_{\mathrm{sat}}\right) \nabla\psi \cdot \mathbf{n} \mathrm{dS} + \int_{S_D} \psi \alpha_{\mathrm{diff}} \left(c - c_{\mathrm{sat}}\right) \mathrm{dS}$$
$$= -\int_{S_J} \left(\mathbf{J} \cdot \mathbf{n}\right) \psi \mathrm{dS} + \int_{S_A} c_{\mathrm{solid}} \mathrm{V_n} \psi \mathrm{dS} \tag{29}$$

with prescribed concentrations or prescribed flux as boundary conditions on S_c and S_J, respectively. Furthermore, S_A and S_D indicate the pit front sections with activation and diffusion control, respectively, and α_{diff} is a stabilization parameter, which should be chosen sufficiently large.

In the case of implicit time integration, the discretized elemental stiffness contribution from domain Ω_P is given by:

$$\mathbf{K}_{\mathrm{Diff}} = \frac{1}{\Delta t} \int_{\Omega_P} \mathbf{N}^{\mathrm{T}} \mathbf{N} \mathrm{d}\Omega + \int_{\Omega_P} \mathbf{B}^{\mathrm{T}} D \mathbf{B} \mathrm{d}\Omega \tag{30}$$

and the discretized element external vector contribution by:

$$\mathbf{f}_{\mathrm{Diff}} = \frac{1}{\Delta t} \int_{\Omega_P} \left(\mathbf{N}^{\mathrm{T}} \mathbf{N}\right) \mathbf{c}^{t-\Delta t} \mathrm{d}\Omega - \int_{S_J} \mathbf{N}^{\mathrm{T}} \mathbf{n}^{\mathrm{T}} \mathbf{J} \mathrm{dS}, \tag{31}$$

where $\mathbf{c}^{t-\Delta t}$ is the concentration in the previous time step. The discretized Robin boundary elemental stiffness contribution is given by:

$$\mathbf{K}_{\mathrm{Diff}}^{\mathrm{Robin}} = \int_{S_A} \mathbf{N}^{\mathrm{T}} \mathbf{N} \mathrm{V_n} \mathrm{dS} \tag{32}$$

and the Robin boundary external vector contribution is defined as:

$$\mathbf{f}_{\mathrm{Diff}}^{\mathrm{Robin}} = \int_{S_A} \mathbf{N}^{\mathrm{T}} c_{\mathrm{solid}} \mathrm{V_n} \mathrm{dS}. \tag{33}$$

The discretized stiffness and external load vector contributions due to the Nitsche boundary are given by:

$$\mathbf{K}_{\mathrm{Diff}}^{\mathrm{Flux}} = -\int_{S_D} D\mathbf{N}^{\mathrm{T}} \mathbf{n}^{\mathrm{T}} \mathbf{B} + D\mathbf{B}^{\mathrm{T}} \mathbf{n} \mathbf{N} \mathrm{dS}, \tag{34}$$

$$\mathbf{K}_{\mathrm{Diff}}^{\mathrm{Stab}} = \int_{S_D} \mathbf{N}^{\mathrm{T}} \alpha_{\mathrm{diff}} \mathbf{N} \mathrm{dS}, \tag{35}$$

$$\mathbf{f}_{\mathrm{Diff}}^{\mathrm{Flux}} = -\int_{S_D} D\mathbf{B}^{\mathrm{T}} \mathbf{n} c_{\mathrm{sat}} \mathrm{dS}, \tag{36}$$

$$\mathbf{f}_{\mathrm{Diff}}^{\mathrm{Stab}} = \int_{S_D} \alpha_{\mathrm{diff}} \mathbf{N}^{\mathrm{T}} c_{\mathrm{sat}} \mathrm{dS}. \tag{37}$$

5.5 | Velocity extension

For the velocity extension from the front to the nodes, the following equation should hold throughout the domain:

$$\nabla V_{\mathrm{n}} \cdot \boldsymbol{\nabla} \phi = 0. \tag{38}$$

As indicated in the flow diagram in Figure 4, the velocity extension is done in two steps. First, the velocity from the front is extended to the front nodes, followed by the velocity extension from the front nodes to the rest of the band domain.

The reason for this is that there is a degree of nonuniqueness in the extension from the front to the front nodes, which is minimized with applying the appropriate boundary conditions. Therefore, before applying the extension to the rest of the domain, the velocity in the front nodes are checked to ensure that the velocity value lies within the velocity range of the adjacent front segments. If this is not the case, it is assigned the maximum or minimum front velocity of the adjacent segments.

For the velocity extension from the corrosion front to the front nodes, the penalty method is used to enforce the boundary conditions on the front. The weak form of Equation (38) in combination with the penalty method becomes:

$$\int_{\Omega_{\text{int}}} (\nabla V_{\text{n}} \nabla \phi)\,(\nabla \psi \nabla \phi)\, d\Omega + \int_{\text{S}} \psi \alpha_{\text{Vel}}\,(V_{\text{n}} - V_{\text{front}})\, \text{dS} = 0, \tag{39}$$

where α_{Vel} is the penalty parameter, which should be chosen sufficiently large, and V_{front} is the front velocity which can differ in value for each front integration point. Note that at this stage ϕ is a known quantity.

The discretized elemental contribution to the stiffness matrix and the external force vector belonging to velocity extension with the penalty method are given by:

$$\mathbf{K}_{\text{Vel}} = \int_{\Omega_{\text{int}}} \mathbf{B}^{\text{T}} \boldsymbol{\nabla} \phi (\boldsymbol{\nabla} \phi)^{\text{T}} \mathbf{B} \text{d}\Omega, \tag{40}$$

$$\mathbf{K}_{\text{Vel}}^{\text{Pen}} = \int_{\text{S}} \mathbf{N}^{\text{T}} \alpha_{\text{Vel}} \mathbf{N} \text{dS}, \tag{41}$$

$$\mathbf{f}_{\text{Vel}}^{\text{Pen}} = \int_{\text{S}} \alpha_{\text{Vel}} \mathbf{N}^{\text{T}} V_{\text{front}} \text{dS}. \tag{42}$$

Due to the ability to have passivation, diffusion control and activation control at the same time at different front integration points, velocity jumps along the front may occur. The front velocity is therefore smeared out by adding a diffusive term to the velocity extension stiffness matrix to improve robustness[45]:

$$\mathbf{K}_{\text{vel}}^{\text{Smear}} = \int_{\text{S}} \kappa h^2 \mathbf{B}^{\text{T}} \mathbf{s}\mathbf{s}^{\text{T}} \mathbf{B} \text{dS}, \tag{43}$$

where $\mathbf{s}$ is a unit vector perpendicular to $\mathbf{n}$, κ is the front stabilization parameter and h is the size of a typical element.

The same field equation is solved once more, but now on the band domain Ω_ϕ instead of just Ω_{int} and with the nodal velocities in Ω_{int} as Dirichlet boundary condition.

6 | NUMERICAL EXAMPLES

Four different numerical examples are considered. First, a basic 1D pencil test is compared with an analytical model. Second, two different initial notches are investigated for different current densities in a two-dimensional (2D) problem. Third, lacy cover formation is modeled for a 2D pit. All these cases do not involve an applied mechanical load. The fourth example shows the behavior of the numerical model when considering pit growth under various electrochemical and mechanical loading combinations. In all examples, the solid material is a 304L stainless steel, which has been chosen because of the available experimental data in literature. Although this material is not used in offshore wind turbines, the principles explained in this article are not material dependent, only the material parameters itself. The model input parameters used throughout all of these examples are given in Table 1, where the values of c_{sat} and D belong to a temperature of 288.15 K. The mechanical material parameters are taken from Antunes et al.[46]

6.1 | 1D pencil test

The specimen geometry and the boundary conditions used for the pencil are shown in Figure 6(A). Geometry and boundary conditions are formulated such that this is a 1D problem, but to test the present framework, it is modeled in 2D here. In this example, it is assumed that the pit front is moving solely under diffusion control, and therefore no value of i_{A} is required. A comparison in pit growth velocity between the numerical model and an analytical relation[7]

TABLE 1 Model parameters

c_{sol}[47]	c_{sat}[9]	D[9]	T	R	F
143×10^{-6} mol mm^{-3}	4.22×10^{-6} mol mm^{-3}	0.575×10^{-3} mm^2/s	288.15 K	8.314 J K^{-1} mol^{-1}	96485.3 C mol^{-1}

z[6]	V_m[6]	E	ν	σ_0	ϵ_0	Q_∞	b	C	γ
2.19	7049.24 mm^3/mol	200 GPa	0.29	117 MPa	0.585E-3	87 MPa	9	52.8 GPa	300

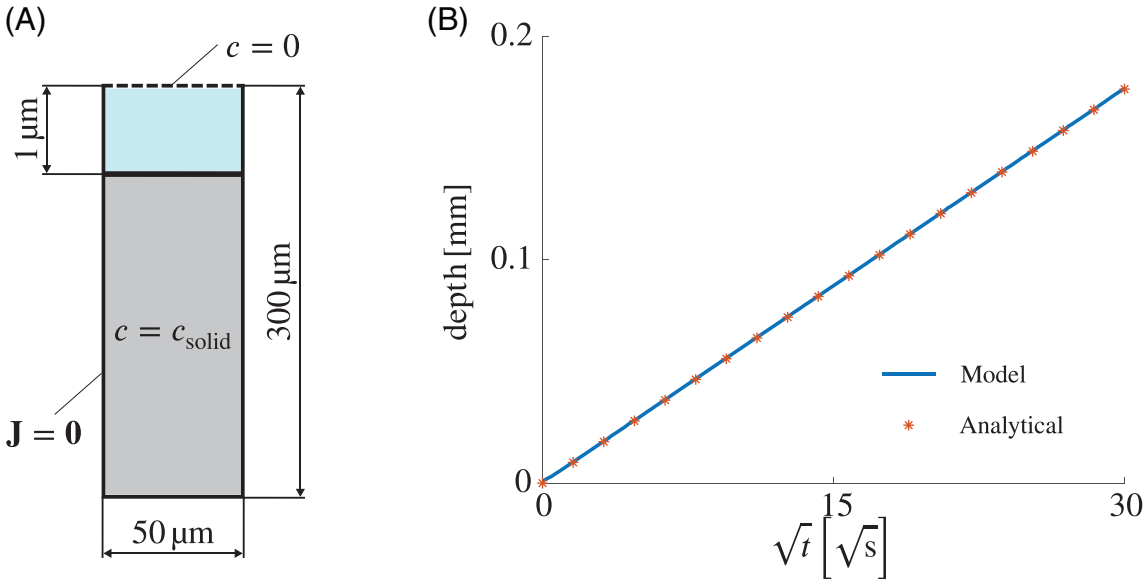

FIGURE 6 (A) One-dimensional pencil test geometry and boundary conditions and (B) comparison of pit growth velocity between the numerical model and an analytical relation in the case of diffusion controlled corrosion

is given in Figure 6(B). It shows that the model prediction and the analytical relation are equal. The mesh size was set to 2 µm.

6.2 | Initial pit shape

A benefit of the level set method is that it can deal with sharp fronts, as well as merging and branching without any special treatment. To illustrate this, two different initial pit shapes are considered: a sharp notch and a double circular pit. The pit boundary nodes along the free surface are assigned a concentration of zero as a Dirichlet boundary condition. Furthermore, the propagation of both initial shapes is studied for a current density of 1 mA mm^{-2} as well as 10 mA mm^{-2} in order to show the difference in shape evolution between activation and diffusion control. Note that in these analyses the possibility of passivation has been switched off. When there is both diffusion and activation control present, Equation (43) has been used to avoid a velocity jump at the intersection of the two types of control. The specimen has a height of 200 µm and a width of 400 µm. The mesh size was set to 2 µm.

Figure 7 shows the initial sharp notch, with a base of 20 µm and a height of 50 µm, and its evolution under the two current densities. For the smaller current density, the corrosion process is under pure activation control, which is shown in Figure 7(B). This means the front velocity is constant along the front and thus the notch shape remains relatively constant. For the larger current density, of which the evolution of the shape is given in Figure 7(C), there is a combination of activation and diffusion control. The transition between the two regimes of corrosion is clearly visible through the overhang. Diffusion control is present along the bottom of the pit, at which the concentration is equal to c_{sat}, while the top of the pit, which is in closer contact with the pit boundary, is under activation control. The front velocity for the diffusion control part is largest near the transition point, because of the larger concentration gradients. This velocity is also larger than the activation control velocity, which is the source of the overhang.

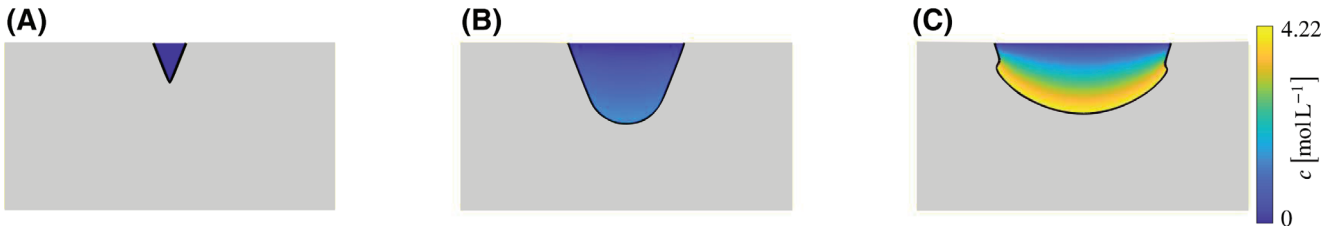

FIGURE 7 (A) Initial V notch and its shape evolution with atom concentration under (B) pure activation control $\left(i_a = 1\ \mathrm{mA/mm^2}\right)$ and (C) a combination of activation and diffusion control $\left(i_a = 10\ \mathrm{mA/mm^2}\right)$

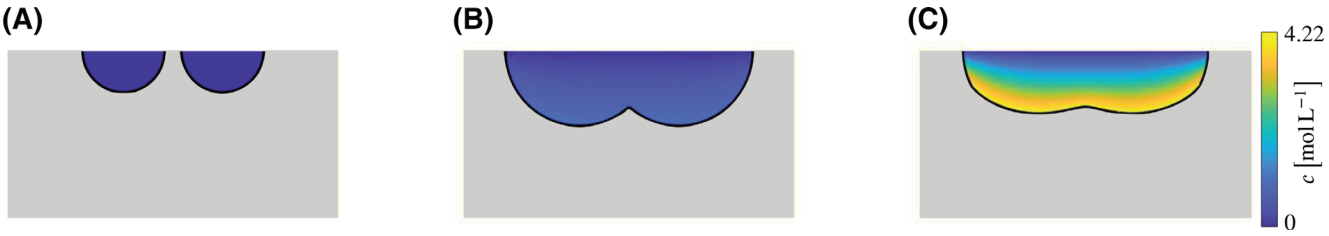

FIGURE 8 (A) Initial two pits and their shape evolution with atom concentration under (B) pure activation control $\left(i_a = 1\ \mathrm{mA/mm^2}\right)$ and (C) a combination of activation and diffusion control $\left(i_a = 10\ \mathrm{mA/mm^2}\right)$

The same type of behavior can be seen Figure 8, which shows the initial double pit shape, with radii 50 μm, and the evolution under the two current densities. For the smaller current density there is again only activation control, which can be seen from Figure 8(B) where c_{sat} is not reached at any point on the pit front. Furthermore, the line of merging is clearly visible because of the sharp tip. For the larger current density, there is again a combination of activation and diffusion control, as shown in Figure 8(C). The overhangs at the transition between the two regimes are not as pronounced as for the sharp notch because of the presence of curvature. The sharp tip at the merging line is smeared out because of diffusion control.

6.3 | Lacy cover formation

The numerical model is compared against experimental data for a corrosion pit with lacy cover[6] in terms of width and depth. A 2D pit is considered with an initial radius R_{init} of 20 μm as visualized in Figure 9(A). The initial concentration of metal ions in the pit is equal to the saturation concentration. The pit boundary nodes are assigned a concentration of zero as a Dirichlet boundary condition. Note that these are only the nodes for which $\phi < 0$ holds. The anodic current density is equal to $i_A = 38\ \mathrm{mA/mm^2}$. The specimen has a height of 240 μm and a width of 800 μm. Only half of the domain of the pit is modeled. In order to accurately capture the formation of the lacy cover, the mesh resolution should be sufficiently small to reduce mesh sensitivity. An unstructured mesh was used with an element size of 0.5 μm at the top, which is where the cover forms, and 2 μm at the bottom of the geometry.

In the numerical model, a lacy cover is automatically formed when including all three different regimes of corrosion into the pit growth computation as is shown in Figure 9(B). The metal atom concentration near the upper part of the pit is lower than the passivation concentration, which means that at these points the front does not propagate. However, at some point deeper into the pit, the passivation criterion is not satisfied any longer. Consequently, the pit front propagates underneath the surface until it reaches the outside environment again and a little island of metal remains. This process is constantly repeated, which is the origin of the lacy cover as observed as a perforated surface layer seen in experiments.[6]

In order to obtain a good agreement with the experiment, it was found that c_{pas} should be set equal to 3 mol L^{-1}, which falls within the range of 50%–80% of the saturation concentration as mentioned by Laycock and White.[10] A lower value for c_{pas} results in a pit width that is too large and a higher value in a too small size. Figure 10(A) shows the comparison between the numerical model and the experimental data. The largest distance from the center line of the pit to a point in the pit that is in contact with the outside environment is defined as the width of the pit. Furthermore,

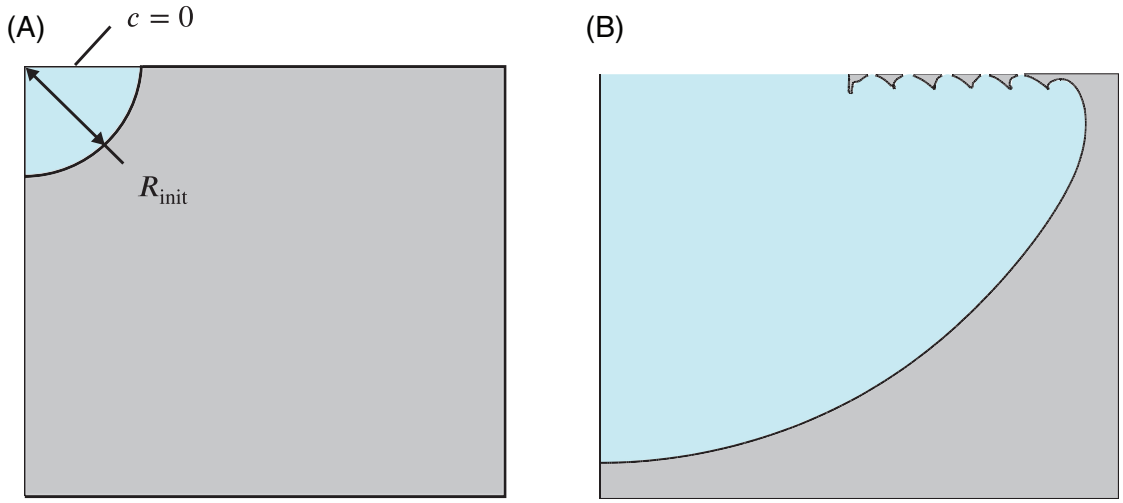

FIGURE 9 (A) Lacy cover specimen and (B) a zoomed in view of the automatic lacy cover formation

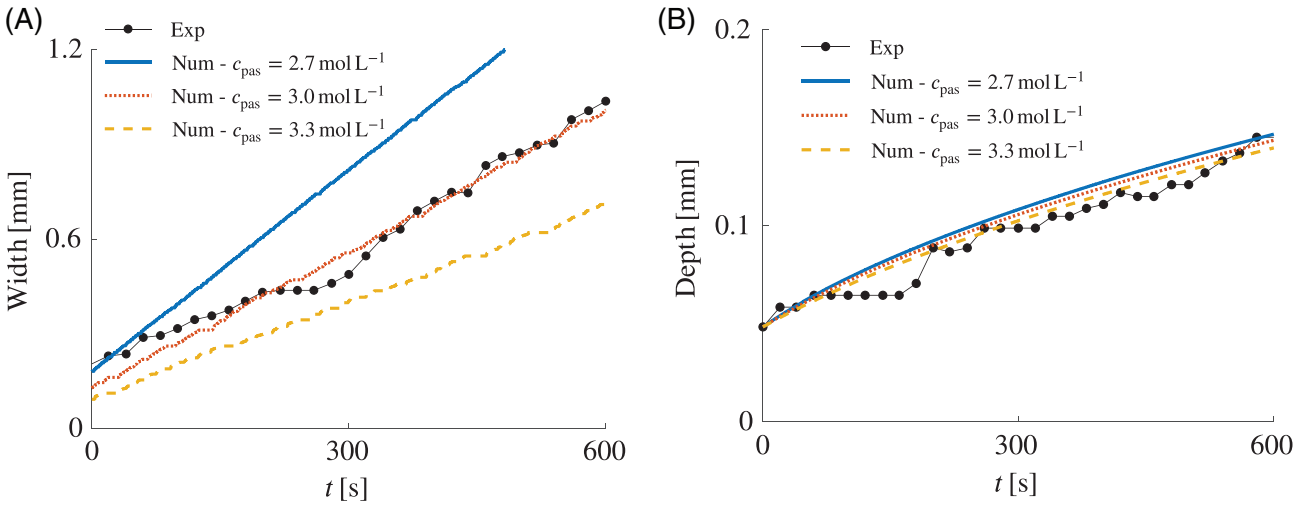

FIGURE 10 Comparison of (A) the width and (B) the depth of two-dimensional pit numerical analyses (Num) with passivation for different c_{pas} against experiment (Exp)

Figure 10(B) gives the comparison of the pit depth, which shows that there is a small dependency of the depth with respect to c_{pas}. A higher c_{pas} reduces the metal concentration gradient and therefore the pit propagation speed at the bottom of the pit.

6.4 | Influence of mechanical load

The influence of mechanical loading on the pit growth behavior is studied using the specimen given in Figure 11 for which the condition of plane stress has been used. The specimen width and height are equal to 800 and 400 μm, respectively. Furthermore, the initial pit radius is 50 μm. The mesh size was set to 2 μm and the length scale r_w from Equation (26) equal to 4 μm. The dashed line, which indicates the presence of a notch, shows the general evolution of the shape of a pit under mechanical loading having a circle as initial pit shape. The notch is formed at the bottom of the pit because it is subjected to the highest amount of stress and thus experiences the highest increase in front velocity. Due to this notch, there is an increase in stress concentration,[48] which further accelerates the growth of the notch. Passivation is not considered in this study.

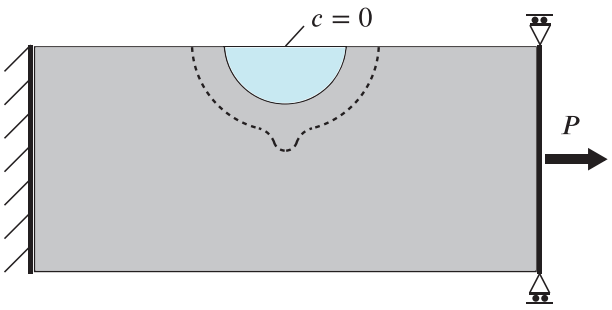

FIGURE 11 Mechanical stress assisted pit growth specimen. The dashed line indicates the evolution of the pit shape

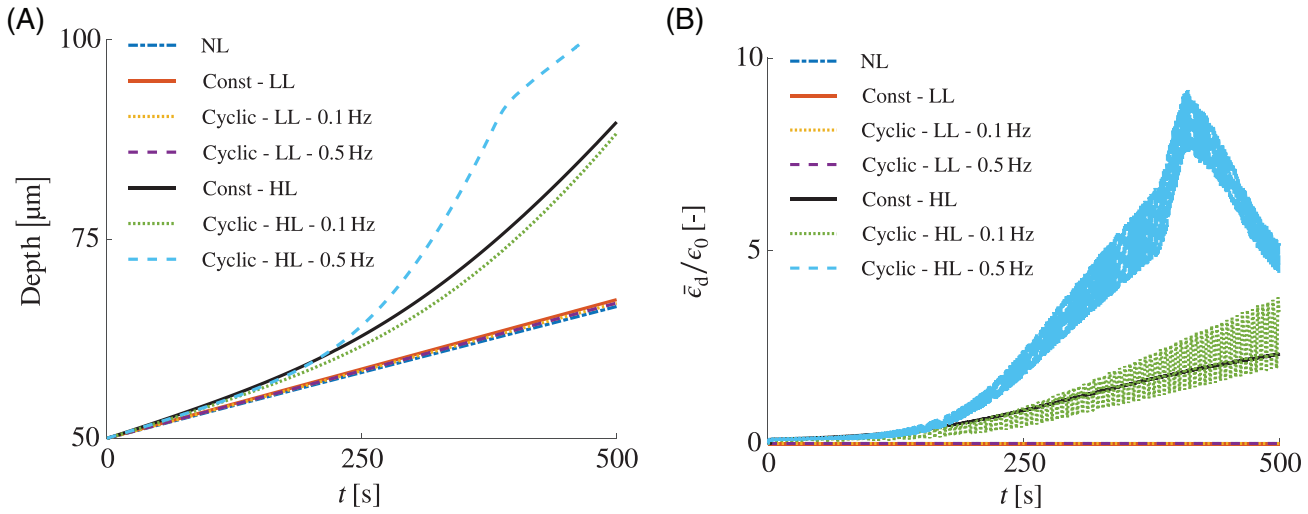

FIGURE 12 (A) Pit depth and (B) equivalent dislocation strain over time for $i_a = 1\text{mA/mm}^2$

Figure 12(A) shows the pit depth and Figure 12(B) the equivalent dislocation strain for simulations under a low current density of $i_A = 1$ mA/mm^2 in the case without mechanical loading (NL), constant applied loading (Const), and cyclic loading (Cyclic) with a load ratio of −1 for different maximum loads and different cyclic load frequencies. The low (LL) and high (HL) maximum loads are equal to 7 and 18 N mm^{-1}, respectively. It can be seen that the pit without mechanical loading is growing slowest. For the low applied load, plasticity is not present. In this case, the pit grows faster under a constant applied loading as compared with cyclic loading, because the hydrostatic stress, which increases the corrosion speed according to Equation (13), is always at its maximum, unlike under cyclic loading. Furthermore, for the low load there is no difference in pit growth for different load frequencies, because the percentage of time that is spent at a certain load is the same.

This is different for the high maximum applied load, due to the presence of plasticity. The high frequency cyclic load case results in significantly faster pit growth compared with the low frequency cyclic load case and the constant load case. This is due to the accumulation of the equivalent dislocation strain due to cyclic hardening. The effect becomes apparent after around 200 s, when a notch starts to develop (see Figure 11) at the bottom of the pit which increases the stress concentration.[48] This increases the stress amplitude and therefore also the effect of kinematic hardening. Interestingly, under a constant load case the pit grows faster than under a cyclic load with a low frequency. In the case of the low frequency there is less time to available for $\bar{\epsilon}_d$ to increase, because the material is already corroded before it can reach its potential maximum. However, the low frequency cyclic load case comes closer to the constant load case over time. This is explained again through the change in shape of the pit, the stress at the pit bottom increases and thus also the built up of $\bar{\epsilon}_d$.

Note that $\bar{\epsilon}_d$ is increasing and decreasing over time for the cyclic load cases according to its definition given in Equation (14). In addition, for the high frequency cyclic load there is a change in behavior around 380 s, which is due to the switch from activation to diffusion control at the bottom of the notch. As could be seen in Section 6.2, diffusion control reduces the curvature of a pit. Consequently, a flatter pit means a smaller stress concentration and thus a decrease of $\bar{\epsilon}_d$ as the pit grows.

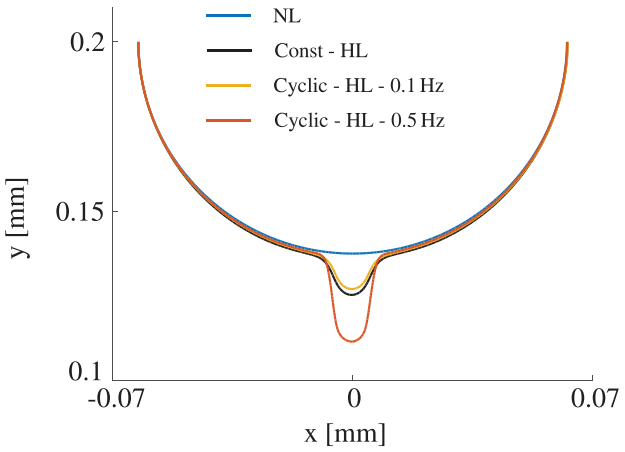

FIGURE 13 Shape of pit at $t = 350$ s for different load cases for $i_A = 1$ mA/mm^2

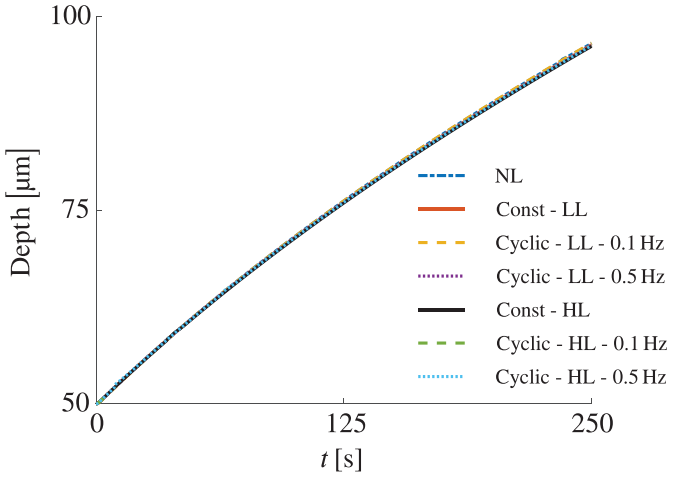

FIGURE 14 Pit depth over time for $i_A = 10$ mA/mm^2

A comparison between the shape of the pit for the high maximum applied load cases and without mechanical load is given in Figure 13. The pits under a mechanical load develop a notch at the pit bottom. It is not difficult to imagine that such notch is a precursor for crack initiation. Furthermore, it can be seen that for the high frequency cyclic load case the notch forming grows faster with time. The cause is again kinematic hardening, which leads to earlier notch forming, which results in a reduction in stress and therefore in corrosion rate at the rest of the pit front.

Finally, the simulations are repeated with a larger anodic current density of $i_A = 10$ mA/mm^2. Figure 14 shows a comparison of the pit depth for the different load scenarios. For all simulations the bottom of the pit is under diffusion control, which implies that mechanical loading does not affect the pit growth rate at these locations and results are the same. However, it can be questioned whether this is realistic, because the salt layer, causing the diffusion control phenomenon, might break down in the case of mechanical loading. Upon break down, larger pit growth rates may be expected as the problem is no longer controlled by diffusion but by activation.

7 | CONCLUSIONS

This study presented a numerical 2D model for corrosion pit propagation under mechanical loading. The level set method was used to track the pit front and to split the domain into a solid domain and a pit domain. The field equations used for the level set reinitialization as well as the velocity extension enable the model to be extended for the use of different mesh types and also three-dimensional analyses.

In the pit domain the diffusion of the concentration of atoms is simulated. The atoms originate from the dissolution process occurring at the pit front. The equilibrium between the propagation velocity of the pit front and the flux through dissolution is defined by the Rankine-Hugoniot front condition. The implementation of the front conditions depends

on the regime of corrosion, which can be activation control, diffusion control, or passivation. These three regimes are required in order to simulate the formation of a lacy cover.

In the solid domain static equilibrium is solved to obtain the strains and stresses. Because the equivalent plastic strain grows indefinitely under cyclic loading, which is physically unrealistic, a new parameter called the equivalent dislocation strain, that depends on the signs of the plastic strain increment and the back stress, was introduced. The new state variable shows a better match with theoretical understanding of how dislocation pile-ups evolve under cyclic loading. However, it still needs to be validated quantitatively.

According to the implemented model a combination of activation control and an elastic material response, results in faster pit propagation under constant amplitude loading than under cyclic loading given the same maximum load. However, in the presence of plastic deformation, cyclic loading can significantly increase the pit growth rate. Furthermore, increasing the cyclic load frequency results in faster pit propagation as there are more cycles to built up plastic strain to kinematic hardening before the material is dissolved into the pit. In the case of diffusion control, mechanical loading does not influence the pit growth rate, provided that the salt layer leading to diffusion control remains intact.

ACKNOWLEDGMENTS

This research is part of the EUROS program, which is supported by NWO domain Applied and Engineering Sciences and partly funded by the Ministry of Economic Affairs.

DATA AVAILABILITY STATEMENT

The data that support the findings of this study are available from the corresponding author upon reasonable request.

ORCID

Richard Dekker https://orcid.org/0000-0002-0054-1400
Frans P. van der Meer https://orcid.org/0000-0002-6691-1259

REFERENCES

1. McCafferty E. *Introduction to Corrosion Science*. Berlin, Germany: Springer Science & Business Media; 2010.
2. Frankel GS. Pitting corrosion of metals: a review of the critical factors. *J Electrochem Soc*. 1998;145:2186-2198.
3. Zhang GA, Cheng YF. Localized corrosion of carbon steel in a CO2-saturated oilfield formation water. *Electrochim Acta*. 2011;56(3):1676-1685.
4. Melchers RE. Pitting corrosion of mild steel in marine immersion environment–Part 1: maximum pit depth. *Corrosion*. 2004;60(9):824-836.
5. Kondo Y. Prediction of fatigue crack initiation life based on pit growth. *Corrosion*. 1989;45(1):7-11.
6. Ernst P, Newman RC. Pit growth studies in stainless steel foils. I. introduction and pit growth kinetics. *Corros Sci*. 2002;44:927-941.
7. Scheiner S, Hellmich C. Stable pitting corrosion of stainless steel as diffusion-controlled dissolution process with a sharp moving electrode boundary. *Corros Sci*. 2007;49(2):319-346.
8. Scheiner S, Hellmich C. Finite volume model for diffusion- and activation-controlled pitting corrosion of stainless steel. *Comput Methods Appl Mech Eng*. 2009;198:2898-2910.
9. Laycock NJ, Newman RC. Temperature dependence of pitting potentials for austenitic stainless steels above their critical pitting temperature. *Corros Sci*. 1998;40(6):887-902.
10. Laycock NJ, White SP. Computer simulation of single pit propagation in stainless steel under potentiostatic control. *J Electrochem Soc*. 2001;148:B264-B275.
11. Sarkar S, Warner JE, Aquino W. A numerical framework for the modeling of corrosive dissolution. *Corros Sci*. 2012;65:502-511.
12. Duddu R. Numerical modeling of corrosion pit propagation using the combined extended finite element and level set method. *Comput Mech*. 2014;54:613-627.
13. Vagbharathi AS, Gopalakrishnan S. An extended finite-element model coupled with level set method for analysis of growth of corrosion pits in metallic structures. *Proc Royal Soc A Math Phys Eng Sci*. 2014;470(20140001):1-27.
14. Duddu R, Kota N a, Qidwai SM. An extended finite element method based approach for modeling crevice and pitting corrosion. *J Appl Mech*. 2016;83(8):05, 081003.
15. Mai W, Soghrati S, Buchheit RG. A phase field model for simulating the pitting corrosion. *Corros Sci*. 2016;110:157-166.
16. Mai W, Soghrati S. A phase field model for simulating the stress corrosion cracking initiated from pits. *Corros Sci*. 2017;125:87-98.
17. Mai W, Soghrati S. New phase field model for simulating galvanic and pitting corrosion processes. *Electrochim Acta*. 2018;260:290-304.
18. Lin C, Ruan H, Shi S. Phase field study of mechanico-electrochemical corrosion. *Electrochim Acta*. 2019;310:240-255.
19. Jafarzadeh S, Chen Z, Zhao J, Bobaru F. Pitting, lacy covers, and pit merger in stainless steel: 3d peridynamic models. *Corrosion Science*. 2019;150:17-31.
20. Wang H, Han E. Simulation of metastable corrosion pit development under mechanical stress. *Electrochim Acta*. 2013;90:128-134.

21. Fatoba OO, Leiva-Garcia R, Lishchuk SV, Larrosa NO, Akid R. Simulation of stress-assisted localised corrosion using a cellular automaton finite element approach. *Corros Sci*. 2018;137:83-97.
22. Lin C, Ruan H. Multi-phase-field modeling of localized corrosion involving galvanic pitting and mechano-electrochemical coupling. *Corros Sci*. 2020;177.
23. Gutman EM. *Mechanochemistry of Materials*. Cambridge, MA: Cambridge International Science Publishing; 1998.
24. Osher S, Sethian JA. Fronts propagating with curvature-dependent speed: algorithms based on Hamilton-Jacobi formulations. *J Comput Phys*. 1988;79:12-49.
25. Hansbo A, Hansbo P. An unfitted finite element method, based on Nitsche's method, for elliptic interface problems. *Comput Methods Appl Mech Eng*. 2002;191:5537-5552.
26. Mergheim J, Kuhl E, Steinmann P. A finite element method for the computational modelling of cohesive cracks. *Int J Numer Methods Eng*. 2005;63(2):276-289.
27. van der Meer FP, Sluys LJ. A phantom node formulation with mixed mode cohesive law for splitting in laminates. *Int J Fract*. 2009;158(2):107-124.
28. Sharland SM, Jackson CP, Diver AJ. A finite-element model of the propagation of corrosion crevices and pits. *Corros Sci*. 1989;29(9):1149-1166.
29. Sarkar S, Aquino W. Electroneutrality and ionic interactions in the modeling of mass transport in dilute electrochemical systems. *Electrochim Acta*. 2011;56(24):8969-8978.
30. Sun X, Duddu R. A sequential non-iterative approach for modeling multi-ionic species reactive transport during localized corrosion. *Finite Elem Anal Des*. 2019;166:103318.
31. Mainguy M, Coussy O. Propagation fronts during calcium leaching and chloride penetration. *J Eng Mech*. 2000;126:250-257.
32. Chaboche JL. Constitutive equations for cyclic plasticity and cyclic viscoplasticity. *Int J Plast*. 1989;5(3):247-302.
33. Chaboche JL. On some modifications of kinematic hardening to improve the description of ratchetting effects. *Int J Plast*. 1991;7(7):661-678.
34. Sharland SM, Tasker PW. A mathematical model of crevice and pitting corrosion - I. the physical model. *Corros Sci*. 1988;28:603-620.
35. Colak OU. Kinematic hardening rules for modeling uniaxial and multiaxial ratcheting. *Mater Des*. 2008;29(8):1575-1581.
36. Sethian JA. *Level Set Methods and Fast Marching Methods: Evolving Interfaces in Computational Geometry, Fluid Mechanics, Computer Vision, and Materials Science*. Vol 3. Cambridge, MA: Cambridge university press; 1999.
37. van der Meer FP, Moës N, Sluys LJ. A level set model for delamination - modeling crack growth without cohesive zone or stress singularity. *Eng Fract Mech*. 2012;79:191-212.
38. Adams T, Giani S, Coombs WM. A high-order elliptic PDE based level set reinitialisation method using a discontinuous Galerkin discretisation. *J Comput Phys*. 2019;379:373-391.
39. De Borst R, Crisfield MA, Remmers JJC, Verhoosel CV. *Nonlinear Finite Element Analysis of Solids and Structures*. Hoboken, NJ: John Wiley & Sons; 2012.
40. Belytschko T, Liu WK, Moran B, Elkhodary K. *Nonlinear Finite Elements for Continua and Structures*. Hoboken, NJ: John Wiley & Sons; 2013.
41. Khoei A. *Extended Finite Element Method: Theory and Applications*. Hoboken, NJ: John Wiley & Sons; 2015:1-565.
42. Wells GN, Sluys LJ. A new method for modelling cohesive cracks using finite elements. *Int J Numer Methods Eng*. 2001;50(12):2667-2682.
43. Dekker R, van der Meer FP, Maljaars J, Sluys LJ. A cohesive XFEM model for simulating fatigue crack growth under mixed-mode loading and overloading. *Int J Numer Methods Eng*. 2019;118(10):561-577.
44. Hautefeuille M, Annavarapu C, Dolbow JE. Robust imposition of dirichlet boundary conditions on embedded surfaces. *Int J Numer Methods Eng*. 2012;90:40-64.
45. Latifi M, van der Meer FP, Sluys LJ. A level set model for simulating fatigue-driven delamination in composites. *Int J Fatigue*. 2015;80:434-442.
46. Antunes FV, Ferreira MSC, Branco R, Prates P, Gardin C, Sarrazin-Baudoux C. Fatigue crack growth versus plastic CTOD in the 304L stainless steel. *Eng Fract Mech*. 2019;214:487-503.
47. Gaudet GT, Mo WT, Hatton TA, et al. Mass transfer and electrochemical kinetic interactions in localized pitting corrosion. *AIChE J*. 1986;32(6):949-958.
48. Cerit M, Genel K, Eksi S. Numerical investigation on stress concentration of corrosion pit. *Eng Fail Anal*. 2009;16(7):2467-2472.

How to cite this article: Dekker R, van der Meer FP, Maljaars J, Sluys LJ. A level set model for stress-dependent corrosion pit propagation. *Int J Numer Methods Eng*. 2021;122:2057–2074. https://doi.org/10.1002/nme.6614